# Spatiotemporal instabilities in a Fabry-Pérot resonator filled with sodium vapor

P. La Penna and G. Giusfredi
*Istituto Nazionale di Ottica, Largo Enrico Fermi 6, 50125 Firenze, Italy*
(Received 23 February 1993)

We report on instabilities in the transmitted polarization of a laser beam crossing a planar Fabry-Pérot resonator filled with sodium vapor, at a null magnetic field, when the input field is linearly polarized and tuned near the center of the $D1$ line. We have measured bifurcation diagrams in the input-power–cavity-detuning parameter space at various angles of incidence. The system shows monostability, bistability, and limit cycles in the transmitted polarization. Oscillations appear only when the angle of incidence is different from zero and the oscillation phase changes with the position on the transverse profile. The observed dynamics is explained by a simplified model which accounts for Zeeman and hyperfine pumpings, focusing and defocusing effects, and atomic motion. By means of this model, we have determined the codimensionality of the system within a theory of the dynamical systems.

PACS number(s): 42.65.Pc, 42.65.Jx

## I. INTRODUCTION

In recent years, instability phenomena in nonlinear optics have been the object of many experimental and theoretical studies. In particular, attention is now focused on the spontaneous formation of spatial structures in the transverse profile of laser beams [1,2]. Here we report on pattern formation in a passive optical system. It consists of a Fabry-Pérot (FP) resonator within which sodium vapor (Na) pumped by an externally injected laser beam tuned on the $D1$ line and linearly polarized, acts as the nonlinear medium. In the past, this kind of system [3–9] was used to study the longitudinal effects of absorption and dephasing giving rise to the phenomena of bistability (OB) and tristability (OT). Different from other works [10–18] our Fabry-Pérot resonator has plane mirrors and the external magnetic field is adjusted to zero, in order to avoid any Larmor precession of the atomic spins. In the absence of a buffer gas the field interacts inhomogeneously with the atoms. As a result, our system offers a variety of phenomena such as multistability in the form of combinations of OB, OT, and pitchfork bifurcations. It also shows intrinsic oscillations in the polarization of the output light if the input beam is slightly tilted from normal incidence on the FP resonator.

This variety of phenomena is the result of the inhomogeneous interaction of the two counterpropagating waves in the FP cavity with the four resonances of the $D1$ line. Thus, depending on the laser frequency, these behaviors may be variously traced as consequences of the inhomogeneous Zeeman and hyperfine pumpings produced by the field on the population of the ground state. However, as we will show in this paper, the transverse effects and the transport of spin orientation due to the atomic motion play a dominant role in the oscillatory instabilities.

It is worth mentioning that very similar instabilities, namely drift instabilities in a nonlinear Fabry-Pérot resonator under oblique incidence, have been theoretically predicted for a Kerr medium [19].

We presented the phenomenology in two previous papers [20,21]. Here we focus on the observations in a narrow region of the parameter space, where the dynamics is relatively simple, with the aim of interpreting the self-pulsing phenomena by a simplified model that contains the minimum number of elements sufficient to reach a qualitative agreement with the experiment. In fact we think that a "complete" model, being too complex and even hardly realizable, would not improve the understanding of the relevant mechanisms. We also wish to point out and explain the relevance of the breaking of the spatial symmetry in the onset of the self-pulsing and of a related spatial pattern.

In Secs. II and III, the experimental setup and results are respectively exposed. In Sec. IV, by analyzing the most significant physical features of the system, we propose a simple interpretation of the observed phenomena. In Sec. V, we introduce a specific model which formalizes the previous considerations, we provide numerical simulations, and we compare them with the experimental results. Finally, in Sec. VI, we analyze the codimensionality of our system.

## II. EXPERIMENTAL SETUP

The device used in our experiments is the same used in [20,21]. It consists of a vacuum-sealed stainless-steel cell, with internal mirrors that form the FP interferometer [20]. Two antireflection-coated windows are at the ends. The free spectral range is about 1.15 GHz, the cold-cavity finesse is about 10 (it has decreased from the previous work), and the transmission of the output mirror is about 5%. The mirrors themselves, about 10 cm apart, confine the sodium vapor in the FP cavity; they are mounted with the coatings outside to prevent their damage from sodium and thus the optical thickness of the resonator is about 13 cm. The Na reservoir is contained in a glass tube at the bottom of the FP chamber. Stable alignment of the mirrors and fine tuning of the cavity length ($L$) are provided by deformable bellows, three quartz spacers, and three piezoelectric crystals. By

 

means of three orthogonal Helmholtz coils we can compensate the background magnetic field inside the cavity to within a 10-mG uncertainty by using the sodium itself as a magnetometer.

The resonant "yellow" laser beam is provided by a cw dye laser Coherent Model 599-21. Its frequency detuning from the center of the $D1$ sodium line is measured with the help of a reference Na cell in a double-pass configuration that allows a Doppler-free analysis of the $D1$ resonance.

In our experimental setup (Fig. 1), we prevent reflections from the FP resonator back into the dye laser with a Faraday isolator. The input power of the laser beam is locked to the signal of a wave-form generator by means of an electro-optic modulator and a photodiode both enclosed in a "noise-reduction" loop. At the cavity input the laser field is linearly polarized, and the available power is approximately 70 mW. The laser beam is spatially filtered and collimated by a telescope over the entrance of the cell with a $2w$ diameter of 2.4 mm. With this value, the "Fresnel number" for our Fabry-Pérot cavity is about 19. The incidence angle ($\theta$) of the laser beam on the FP is changed by adjusting the micrometers on which the second lens of the telescope is mounted.

The variations of the cavity length are measured with the help of a frequency stabilized HeNe laser Newport Model NL-1. Its "red" beam is superimposed on the dye laser beam through a polarizing cube splitter. At the output side of the FP, the red beam is separated by the yellow one by an interference filter. The power of the transmitted red light is measured by a photodiode. Its signal is used to stabilize the cavity length against thermal and mechanical fluctuation or to keep the variations of $L$ under control by means of a computer program that calculates the corresponding laser-cavity detuning ($\delta_c$) variations between the yellow beam and the cavity. It must be noted that $\delta_c$ is always measured with reference to the resonant position (for the given value of $\theta$) at very low input power.

At the FP output we also divide the two circularly polarized yellow light components with a circular analyzer. One arm of the two into which the beam is split is used to monitor the power of one circular component with a photodiode. Its signal is sampled by a Le Croy digital oscilloscope together with the signal of the input power ($P_{\text{in}}$) or the signal of the transmitted HeNe beam. Both signals are finally stored and analyzed by a personal computer (PC).

The other arm is used to monitor the transverse profile of the beam intensity or of the oscillation amplitude and phase [22]. For this purpose the beam profile is mechanically sampled by a rotating Nipkow disk having 60 small apertures (200 $\mu$m in diameter) placed along two spirals. Each rotation of the disk produces two sets of interlaced sampled lines across the profile of the beam. The sampled area is about 1 cm$^2$, with a resolution of $64\times60$ pixels. The light transmitted by the disk is detected by a phototube whose signal is first analogically analyzed in different ways. In one case the oscillation amplitude is measured. In the other case, the signal goes through a lock-in that uses as reference the signal detected on the first arm. The time constant of this lock-in circuit is automatically adapted to the oscillation frequency. In this way, it is possible to have information on the phase relationship of the oscillations at different points of the profile. In both cases the resulting signal is acquired by a Philips, Model PM3320, digital oscilloscope and stored on the PC.

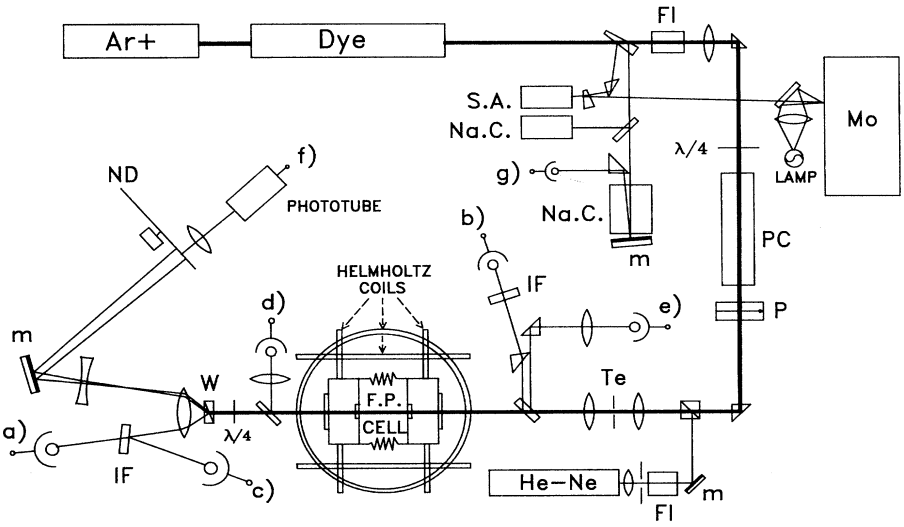


FIG. 1. Experimental setup. Ar+ =Ar-ion pump laser; DYE is the dye laser; FI is the Faraday isolator; $m$ is the mirror; Te is the beam coupling telescope; PC is the Pockels cell; P is the polarizer (horizontally oriented); FP is the Fabry-Pérot cell; W is the Wollaston prism; IF is the interference filter; and ND is the Nipkow disk (for transmitted profile analysis). The laser frequency is monitored on a monochromator (Mo), a spectrum analyzer (SA), and a reference Na cell (Na.C.). (a) and (b) photodiode signals for the stabilization apparatus; (c) photodiode monitoring of total output power; (e) photodiode monitoring the input power ($P_{\text{in}}$); (f) phototube output for profile analysis; and (g) output for frequency definition.

## III. EXPERIMENTAL RESULTS

Several parameters may be varied to characterize our system. We choose to avoid external breaking of the symmetry due to a nonlinear polarization or to a magnetic field as much as possible. Moreover, we limit the analysis to a small region in the sodium-density and laser-frequency-detuning space. To be precise, the results reported here are obtained with Na densities $N$ of about $1.7\times10^{11}$ cm$^{-3}$ (temperature $T=150$ °C) and with a frequency detuning ($\delta_l$) of the laser from the center of the $D1$ line of about $+135$ MHz. Relatively small variations of these two parameters do not change qualitatively the behavior of the system.

The control parameters that are most relevant are the input power $P_{in}$, the laser-cavity detuning $\delta_c$, and the incidence angle $\theta$ of the laser beam with the FP axis.

At the laser frequency and the sodium density just specified, when $P_{in}$ is increased at fixed $\delta_c$ (typically above 0) and $\theta$, the transmitted light shows a transition from a monostable state with linear polarization to a bistable state with almost left or right circular polarization through pitchfork bifurcations (PB's) or through a polarization switching (PS) due to a small tristable hysteresis [5,6]. For different values of $\delta_c$ (typically below 0), the transition is toward a limit cycle through a Hopf bifurcation (HB) (Fig. 2).

The bistable state corresponds to a symmetry breaking in the polarization in which one circular component approaches the cavity resonance and the other component is moved away. The limit cycles appear mainly as polarization oscillations, with the power of the two circular components out of phase with respect to each other, while the total transmitted power shows smaller fluctuations mainly arising from distortion of the oscillations from a sinusoidal form.

When $\delta_c$ is slowly varied, the oscillations start smoothly from the linear polarization state and they end up falling on a left or right polarization state. The opposite

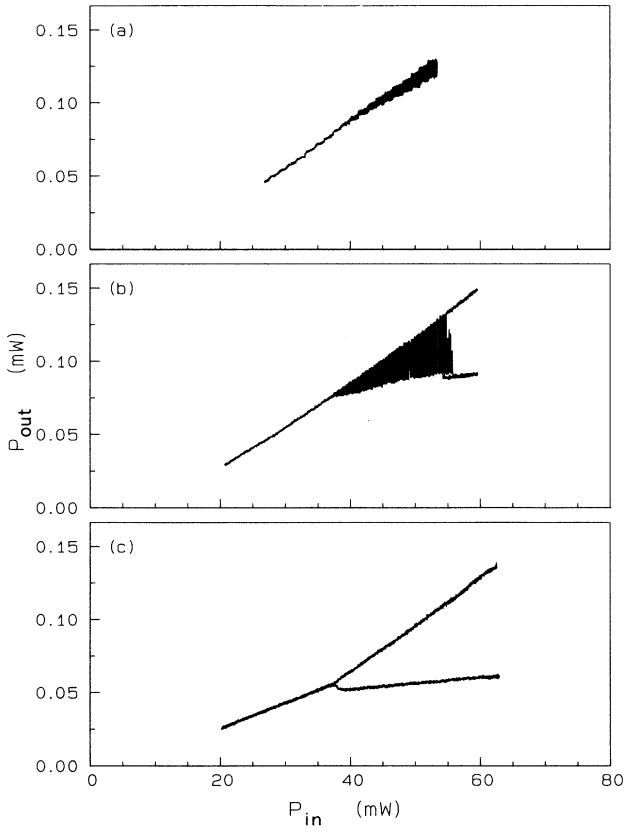


FIG. 2. Output power of one transmitted circular component during a triangular modulation of $P_{in}$, with three different cavity mistunings ($\delta_c$) and for an incidence angle $\theta=0.3$ mrad. (a) $\delta_c=-50$ MHz, Hopf bifurcation (HB): there are oscillations for the whole explored range of $P_{in}$. (b) $\delta_c=8$ MHz, oscillations start and then abruptly cease on a high or low transmission state of the component. (c) $\delta_c=99$ MHz, Pitchfork bifurcation (PB).

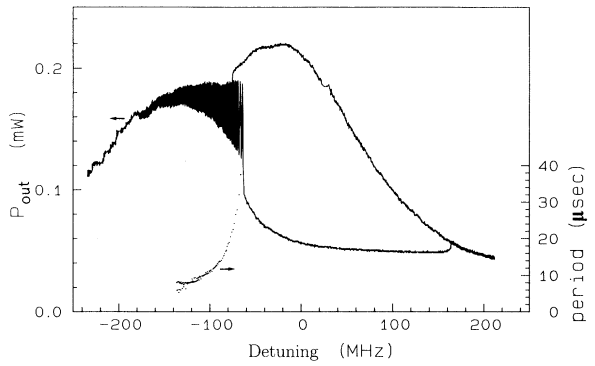


FIG. 3. Output power vs cavity detuning, at fixed $P_{in}\approx50$ mW, for $\theta=0.2$ mrad. In the dotted curve the periods of the oscillations to be read on the left scale are reported.

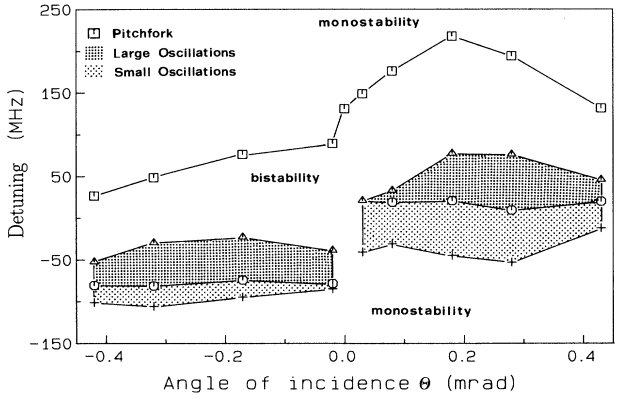


FIG. 4. Phase diagram of the instabilities in the plane of $\theta$ and $\delta_c$, for $P_{in}\approx70$ mW: the sign before $\theta$ means different sides from the aligned position. For $\theta=0$ there are no oscillations and the transmission goes from a linear polarization state (monostability) to a left or right polarization state (bistability). Oscillations occur in a range of $\theta$ of about $\pm0.5$ mrad (shadowed area); there is a region in which they are confused with the noise (small oscillation).

occurs when reversing the scanning: the oscillations, after starting with an abrupt destabilization of the left and right polarization states, smoothly end on the linear state. Usually the amplitude and also the period of the oscillations progressively increase as we proceed away from the HB point and the frequency approaches zero at the falling point, while the shape of the oscillations becomes more and more of the square-wave type. Thus, by acting on the detuning, we can widely change the oscillation frequency in a range from zero up to around 1 MHz (Fig. 3).

A similar behavior may also be observed in the scanning of the input power. In both cases, a small hysteresis is present in going from the oscillations to the stable left or right polarization and back.

An important fact is that the oscillations do not appear for a null value of the angle $\theta$. In other words, a breaking of the axial symmetry is necessary for their existence. Increasing $\theta$, the frequency of the oscillations also increases, while their amplitude decreases. Their presence is limited in an experimentally small range of $\theta$ values: $0 < \theta \leq 1$ mrad (Fig. 4).

However, the various directions in which the beam may be tilted are not all equivalent. Indeed, there is also

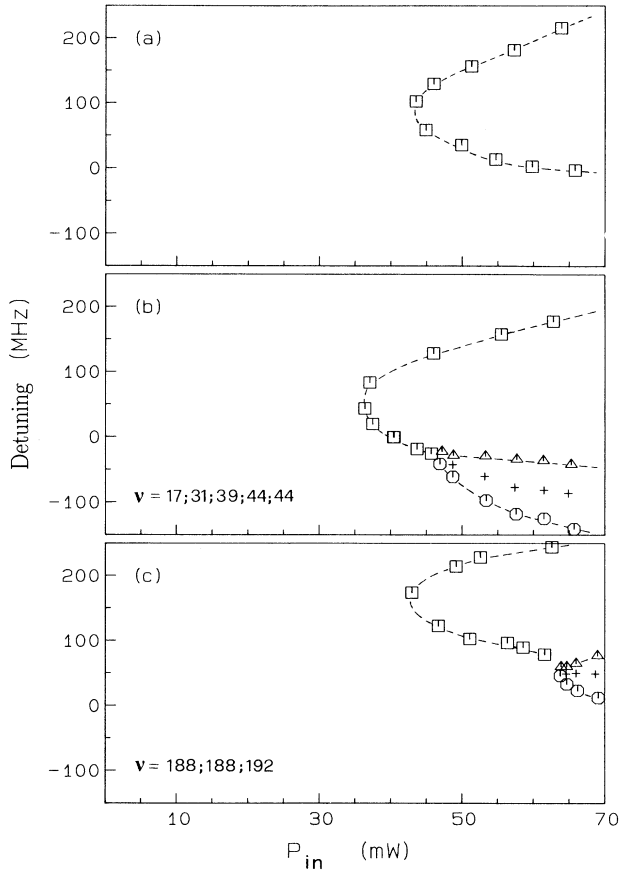


FIG. 5. Experimental bifurcation diagrams, in the plane of $P_{in}$, $\delta_c$, for three different values of $\theta$. (a) $\theta=0$: there are only PB or polarization switchings (PS) (squares). (b) $\theta=0.1$ mrad: for $\delta_c$ less than 0 there is a line of HB (circles) and a line crossing which oscillations cease on a stationary left or right polarization state (triangles). The frequency values (in kHz) shown refer to the crosses inside the region with oscillations, in the same order from left to right. (c) The same as before for a larger $\theta$ value ($\theta=0.35$ mrad): the point of intersection of the bifurcation lines drifts toward higher $P_{in}$ and the oscillations frequency grows.

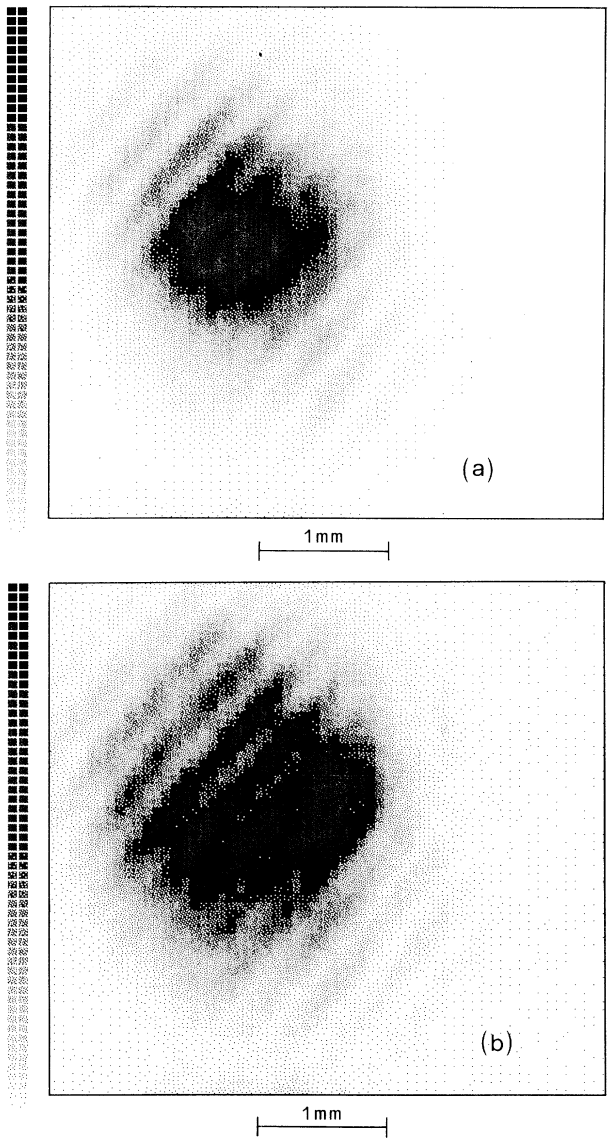


FIG. 6. Transverse near-field profile of a transmitted circular component after a PB or a PS. The images are "negatives" for better representation: darker areas correspond to higher intensities and both have the peak normalized to the same value. The real peak intensity ratio is about 3:1. The bar below these and the following figures refers to the approximate size scale of the near-field beam cross section. (a) The component is on a high transmission state. $P_{in}=14$ mW; $\delta_c=192$ MHz; output power $=0.10$ mW. (b) The same component is now on a low transmission state, for the same parameter values as before. The thin fringe pattern superimposed is due to interference between reflections on the different surfaces of the cavity mirrors.

an internal breaking of the axial O(2) symmetry in our FP. Since the mirrors are mounted with the coatings outside, inside the cavity for each mirror there is a contribution to reflection arising from the internal face of the substrates. A defect of our FP is that one of these faces does not have any more an antireflection coating and the correspondent reflection interferes appreciably with the reflection from the coated side. Because the angle between the two faces is relatively small, a dozen fringes are visible in the transverse profile of the beam transmitted by the FP, and the profile itself is slightly elongated in the direction normal to the fringes. Therefore the symmetry of our system is only reflectional ($Z_2$) across a plane containing the axis of the cell. When the input laser beam is tilted in this direction the oscillatory regime does not appear, while on the contrary it reaches its maximum extension if the tilt is applied in the direction parallel to the fringes. In conclusion, oscillations appear when there is a breaking of the *residual* $Z_2$ symmetry left by the cavity.

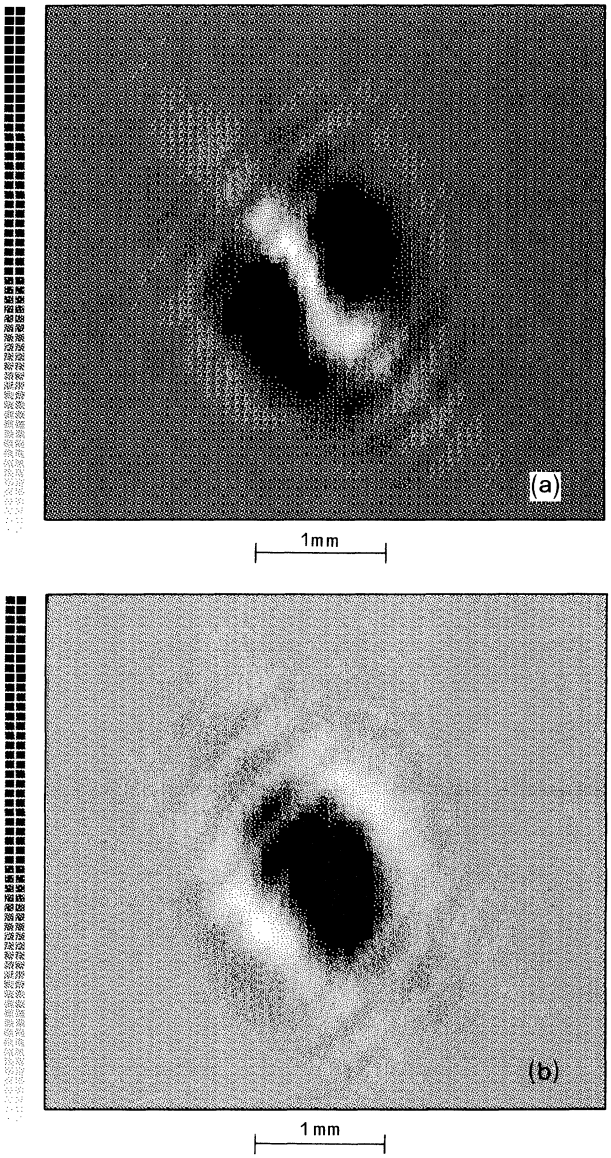


FIG. 7. Transverse profile of a transmitted circular component in the presence of oscillations: phase analysis. The brighter zones are oscillating in opposition of phase to darker ones. The two images (a) and (b) are taken with two phase references which differ in 180°. The "striped" pattern in each image indicates that different zones of the cross section are oscillating with different phases. The spurious fringes of interference of our resonator are also visible: they are fainter, thinner, and perpendicular to the stripe pattern.

Figure 5 shows the bifurcation diagrams obtained for three different values of $\theta$. These diagrams were obtained point by point by varying manually the input power and the cavity detuning. In this way we avoided the effects of unwanted dynamical hysteresis. The discrimination between stable and oscillatory states was obtained with the help of an electronic spectrum analyzer. The discrimination between monostable and bistable states was obtained looking at the difference in power between the two circular components transmitted by the FP. The presence of an intermediate tristable region has not been reported here because OT hysteresis was always very small and confused by noise and by dynamical effects. Therefore a discrimination between PB and PS has not been done.

The transverse profiles of the transmitted beam obtained by using the Nipkow disk show that spatial transverse effects are relevant. In the case of a bistable state, the more transmitted circular component is focused while the less transmitted component is defocused (Fig. 6). Thus the cavity is stable for the more transmitted component and unstable for the other one. This effect adds to the longitudinal dispersive effect in inducing the bistability.

In presence of limit cycles, the phase of the oscillations is not spatially uniform across the section of the beam. Indeed, the phase analysis of Fig. 7 shows a stripe pattern in which the polarization of the bright region is oscillating out of phase with respect to the dark region. As the internal phase reference of the lock-in is varied, the stripes translate continuously. This indicates that the phase of the oscillations changes monotonously in only one transverse direction, therefore the field intensity profile changes continuously in time moving as a wave in that direction. The orientation of the stripes is parallel to the symmetry plane of the cavity and remains almost independent of the orientation of the tilt. In other words, the fringes produced by the mirrors are pronounced enough to guide the spatial evolution of the oscillations.

## IV. DISCUSSION

The atomic motion is free inside the cavity. Indeed, at the working vapor densities, the mean free path of an atom, calculated from elastic and spin exchange cross sections [23], is much longer than the cavity length. Thus the characteristic field-atom interaction time is just the mean transit time across the beam. This is about 5 $\mu$sec, which is much longer than the decay time $\tau$ of the excited state (16 nsec) or the field decay time of the cavity ($\approx$3 nsec) and, for light intensity sufficiently smaller than the saturation intensity of the $D1$ line, the field adiabati-

cally follows the evolution of the ground-state population. The effects of the field itself may be approximately described in terms of hyperfine polarization, spin orientation, and spin alignment of the atoms in the ground state.

The Doppler broadening is much larger than the natural linewidth ($\approx$1500 MHz against 10 MHz) and is comparable to the hyperfine separation (1772 MHz). Each velocity group of the ground-state population has a different dynamics, which in particular depends on the strength of the two competitive laser-atom interactions from the two $F=1,2$ ground-state levels. Each of these two interactions may be approximately described by the sum of four Lorentzian functions $P_{ij}/(1+\Delta^2)$, where $\Delta=2\tau 2\pi(\nu_l \pm v_z/\lambda-\nu_{ij})$ is a normalized detuning, $P_{ij}$ and $\nu_{ij}$ being, respectively, the strengths and frequencies of the four transitions from the ground to the excited states, $\nu_l$ the laser frequency, $v_z$ the longitudinal velocity of the atoms, and $\lambda$ the wavelength.

To check the absorption and dephasing dependence of the vapor on the laser intensity and polarization, we have used the formalism of the irreducible components of the density matrix [24], which we applied with some approximation to the effective structure of the $D1$ line of sodium (Figs. 8–13). The equations used are derived from Eq. I.20 of Ref. [25]. They are solved at equilibrium, taking the relaxation time of the ground state to be equal to the mean transit time through our laser beam. The computation is done in the approximation of an incoherent superposition of the two counterpropagating waves and neglecting the mixed components between the two ground-state hyperfine levels and between the two upper levels. Only a few of the 36 computed irreducible components are represented in the figures, namely atomic populations (${}_F\rho_0^0$), dipoles (${}_F\rho_0^1$), and quadrupoles (${}_F\rho_0^2, {}_F\rho_{\pm 2}^2$) of the two ground-state sublevels (with $F=1,2$).

Let us first consider the effects of two linearly polarized and counterpropagating laser beams. In this case, the hyperfine pumping is the main process. It leads to peaks and dips in the velocity distributions of atomic populations of both $F=1,2$ ground-state levels (Fig. 8). The width of these peaks and dips grows with the laser intensity and, already at moderate values (few mW/mm$^2$ in our geometry), is of the order of the excited-state hyperfine separation (190 MHz). By considering the peak and dip intensity broadening, the structure of the excited state may be neglected; thus with this simplification there are four atomic groups in the velocity distribution that are resonant from the $F=1$ or 2 ground-state level with the forward ($F$) or backward ($B$) wave in the FP cavity. These waves act as pump and probe, one with respect to the other: each wave is essentially absorbed by its resonant groups and dispersively affected by the pumping of the other in its own groups.

In our experiment we kept the laser frequency close to, but not coincident with, the center of the $D1$ line (in particular the closest crossover frequency was about 40 MHz away). In this case, on each side of the velocity distributions there are two close groups in which the atoms are fast pumped from one ground-state level to the other.

The intracavity beam peak intensity, ranging around 2 mW/mm$^2$, is much larger than the saturation intensity for linearly polarized resonant light (0.19 mW/mm$^2$, if the hyperfine structure is totally neglected). However, the resonant atoms are pumped in the other hyperfine sublevel keeping the excited-state level population small.

Those nonresonant atoms, which lay between the close resonant groups in the velocity distribution, are affected by the competition of the two counterpropagating waves that pump in opposite directions. Therefore the hyperfine pumping is less effective on these atoms. Nevertheless, they mainly interact through the excited state $F'=2$, for which there is a nonabsorbing state in the $F=2$ sublevel. So they also accumulate in the $F=2$ state and a spin alignment takes place.

For the atoms that have a longitudinal velocity in the regions between null and "resonant" velocities, with the laser frequency chosen in the present work, the hyperfine pumping is oriented (with much lower pumping rates) from the $F=1$ to the $F=2$ ground-state level. For atoms in the middle of this region, with a Doppler shift of 350 MHz, the rates for the $F=1$ and 2 ground-state levels

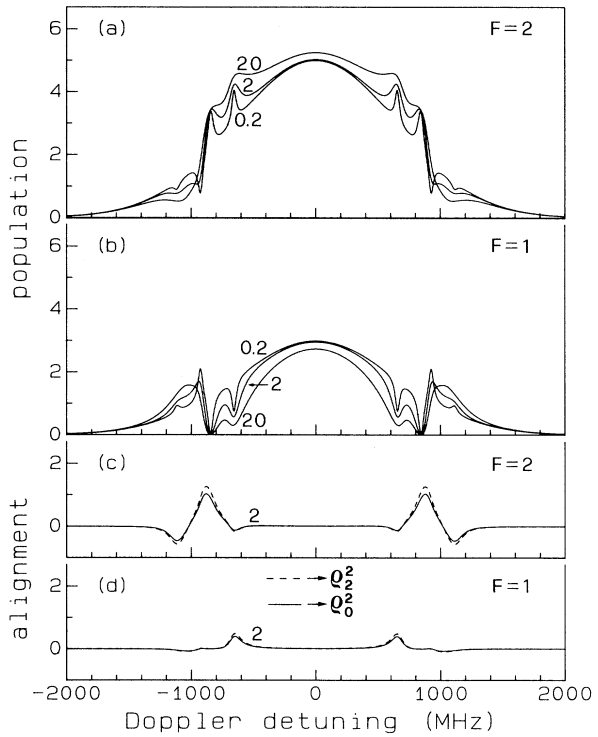


FIG. 8. Ground-state (longitudinal) velocity distributions for the irreducible components (population and alignment) of the density matrix for sodium computed at equilibrium with the whole hyperfine structure of the $D1$ line. The pumping field consists of two equally linearly polarized counterpropagating waves having the same intensity and tuned at +135 MHz from the center of $D1$ line. The relaxation time for the ground state is taken 5 $\mu$sec. Each standard value is multiplied for $8\sqrt{2F+1}$. Here and in the following figures the numbers indicate the (single-wave) pump intensities in mW/mm$^2$.

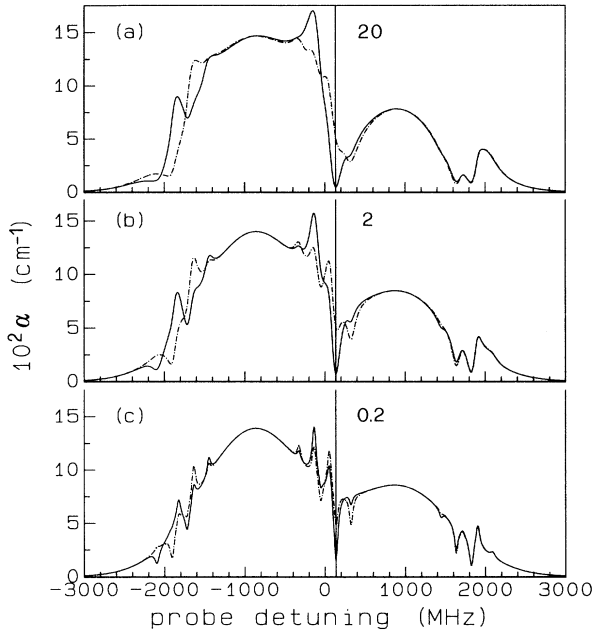


FIG. 9. Imaginary part (absorption) of the propagation eigenvalues for the (two orthogonal) polarization components of a weak probe at the same values of Fig. 8, with a linearly polarized pump, and at 150 °C ($N = 1.7\ 10^{11}$ at./cm$^3$). The vertical line indicates the frequency position of the pump. Continuous line, polarized as the pump; broken line, polarized orthogonally to the pump.

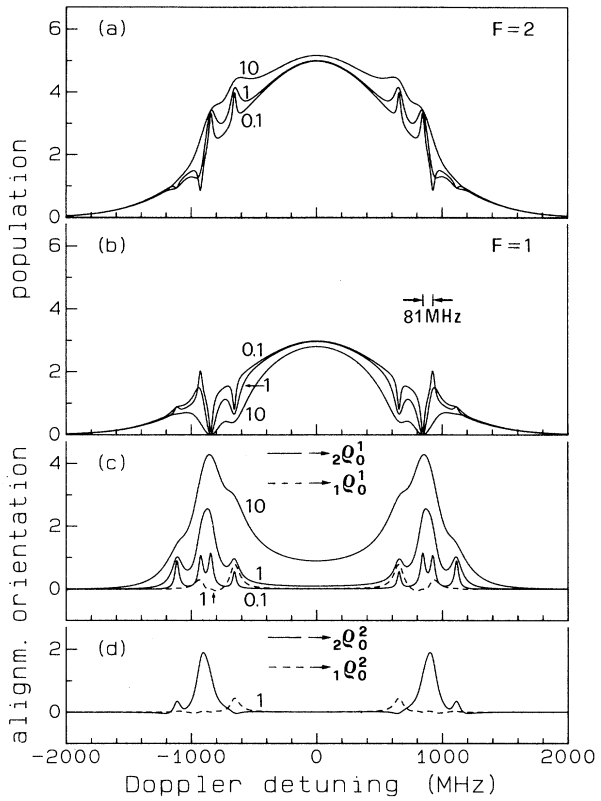


FIG. 11. Ground-state population, orientation, and alignment distributions computed as in Fig. 8, but with a circularly polarized pump.

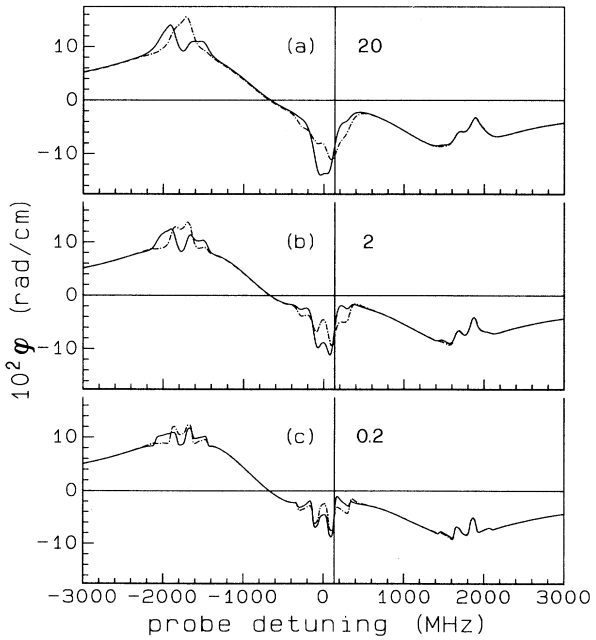


FIG. 10. Real part (dispersion) of the propagation eigenvalues of a weak probe as in Fig. 9.

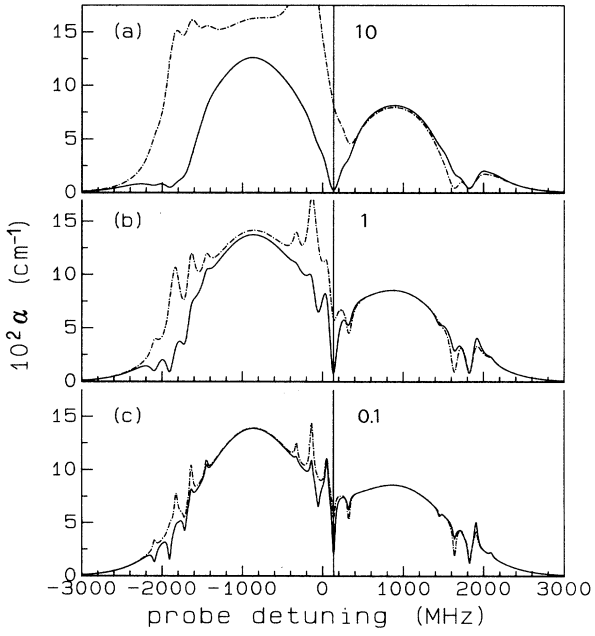


FIG. 12. Imaginary part (absorption) of the propagation eigenvalues of a weak probe as in Fig. 9, but in the presence of a circularly polarized pump.

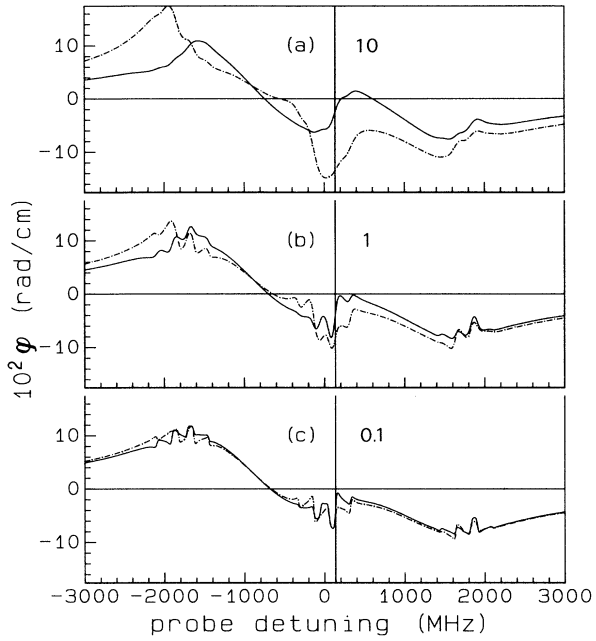


FIG. 13. Real part (dispersion) of the propagation eigenvalues of a weak probe as in Fig. 10, but in the presence of a circularly polarized pump.

are, respectively, about 6400 and 19600 times smaller than the correspondent pumping rates of resonant atoms. Analogously for the atoms in the wings of the distribution, with a velocity higher than the resonant velocity, the hyperfine pumping is oriented from the $F=2$ to the $F=1$ ground level. In our case there is a minority of atoms involved in this way of pumping.

The effect on the field may be analyzed by considering now the atomic population as a function of its detuning with respect to the forward beam. This function is simply the partial overlapping of the rescaled velocity distributions of the two $F=1,2$ levels. By increasing the field intensity, the population on resonance and on its positive frequency side (which belongs mainly to the $F=1$ level) decreases, while the population on the negative sides (which belongs mainly to the $F=2$ level) increases. At equilibrium the absorption and dephasing that would be experienced by a weak probe tuned around the $D1$ line is showed in Figs. 9 and 10, respectively.

When the field polarization is elliptical or circular, Zeeman pumping takes place (Fig. 11). In particular, for circular polarization, all the atomic population is pumped toward one nonabsorbing state with $F=2$ and $m_F=2$ or $m_F=-2$ with an efficiency that depends on the Doppler shift. At a laser detuning of 135 MHz, a rough estimation of a "mean" detuning for the atoms that contribute to the orientation is 50 MHz, to which correspond pumping rates about 100 times smaller than those of the resonant atoms. The effect on the field is that, for elliptical polarization, the strongest circular component "sees" a frequency distribution of the interacting population that decreases when the field intensity is increased. The weaker component sees instead an increase in the population on the negative side, while the population on the positive side decreases. The effects on a weak probe are now shown in Figs. 12 and 13.

In conclusion, we can consider the atomic population as consisting of a part, that contributes to saturable absorption with a fast response and a larger part that contributes to dispersion, but with slower rates. This second part provides a negative dispersion coefficient for both circular components if there is only a hyperfine polarization (Fig. 10), while it provides additional negative and positive dispersion coefficients for the two opposite circular components if there is also a Zeeman polarization (spin orientation) (Fig. 13).

In our case, the Zeeman polarization induces a refraction index that increases with pumping power for the circular component of the light that prevails during the pumping process and instead decreases for the other one. Thus Zeeman pumping, together with spatial dependence of input power, leads to a self-focusing effect for the strongest component and self-defocusing for the other one, as shown by Fig. 6. The effect of hyperfine pumping instead is to induce a refractive index that decreases with the input power for both circular components, thus yielding a contribution to self-defocusing.

Instabilities in this spatial distribution of refractive index can be introduced by a polarization transport phenomenon due to the atomic motion through the laser beam. Particular conditions can exist for which these instabilities lead to an oscillatory behavior in the spatial distribution of refractive index, continuously reshaping the focusing and defocusing effects on the field. In fact, the frequency values of the observed oscillations are close to the inverse of the transit time across the beam. During a period of oscillation, the atomic motion can effectively change the gradient of spin orientation generated by the optical pumping without being so fast as to destroy it. Indeed, the atoms pumped in the center of the beam move toward the periphery, while unpumped atoms enter the beam. Therefore, it is possible that the atomic motion could drive the oscillations with a sort of delayed feedback while the FP cavity could give an amplification of the focusing and defocusing effects induced by the gradient itself.

Thus oscillations in the transmitted light can be thought of as a consequence of the matching of these effects with the stability behavior of the FP cavity when the "right" conditions happen. We have verified the validity of this intuitive hypothesis through numerical simulation of a simplified model.

## V. SIMULATION

An analytical and complete description, in terms of the time evolution of the density matrix, would have to be quite involved to capture the essential physical mechanism of our system. Therefore, we have developed a model that permits a numerical simulation of the atomic motion across the transverse section of the laser beam and of the consequent evolution of the atomic polarizations and beam profile.

In order to obtain an agreement with the experimental results we have found that it is important to compute the transverse profile of the field inside the cavity with good precision, while for the atomic variables it is sufficient to follow the evolution of the Zeeman polarization (orientation) $\langle S_z \rangle$ and the hyperfine polarization $\langle \mathbf{I}\cdot\mathbf{S} \rangle$ in the ground-state level.

This model is in the mean-field approximation, so that the longitudinal dependence is neglected. A further strong simplification introduced in the computation is that the program deals with just one transverse direction (namely $x$), so that the model becomes one dimensional. This simplification makes the computation fast enough for our machine (a computer work station HP 9000/730) and it is suggested by the experimental evidence (as already mentioned) of a symmetry breaking induced by the cavity, which imposes a preferential direction in which the instabilities arise. Furthermore, we assume that only atoms with a definite longitudinal velocity contribute to the Zeeman polarization and atoms with another one contribute to the hyperfine. This might appear to be a severe approximation of how the two pumping processes act on the atomic distribution, but after various attempts it has proved to work well.

The simulation goes on with finite and constant time steps $\Delta t$. The $x$ axis in the model is subdivided, for the atomic evolution, into 128 pixels, each one determining an $x_j$ transverse coordinate. The atoms are considered to be moving along this axis, in the two opposite directions, and the velocity is sampled so that there are *only two* spatial distributions of the atomic polarizations that at each step in time are translated symmetrically in the two opposite directions.

A "diffusive" spreading is superimposed on the translation in order to approximate the Gaussian spreading of an atomic spatial group (Fig. 14). In particular, the spatial polarization corresponding to one pixel and one direction of motion is redistributed partially on the same starting pixel and the rest on the following three pixels with different "weights" (e.g., 37% on the starting interval, 48% on the first one, then 13% and 2%). Thus the superposition of the polarization moving in the two opposite directions gives something like a Maxwellian spreading of the spatial group. However, we have verified that these weights may be widely varied without appreciably affecting the results of the simulation. With the above values, to each time step corresponds a mean displacement of $0.8\Delta x$, where $\Delta x$ is the width of a pixel. Boundary conditions for completely depolarizing collisions with cavity walls are reproduced by introducing unpolarized atoms coming from outside the beam.

Figure 15 summarizes the algorithm. Let us suppose that for a fixed time instant the absorptions and dephasings due to the atomic distributions are already computed. The first step is then to compute the transmitted field in these conditions. This is carried on by means of an iterative method, introducing (for each $x_j$ coordinate) half of the effect of the atoms on the field both before and after the intracavity propagation and finally applying the boundary conditions at the mirrors. At the $(m+1)$th iteration, if $U_m(x)$ is the intracavity field profile at the

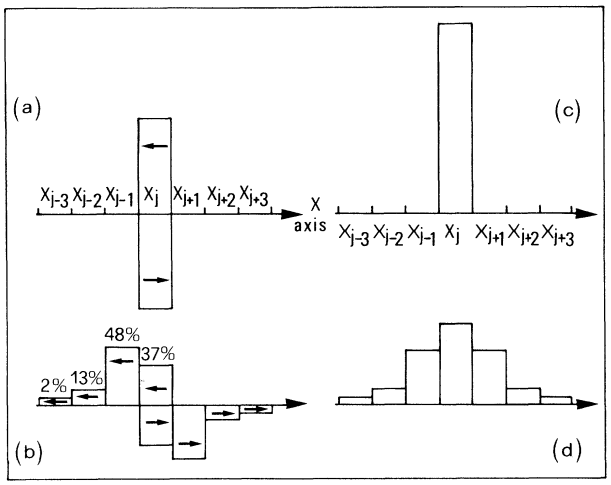


FIG. 14. Spatial redistribution of the atoms after a time step to simulate their motion. In (a) the area of the rectangle represents the population of just one spatial pixel and (b) shows the subsequent redistribution in the adjacent pixels: the two ways of motion are indicated by the arrows and the populations are drawn on the two different sides of the $x$ axis. In (c) and (d) the two packets are overlapped to show the total broadening of the population.

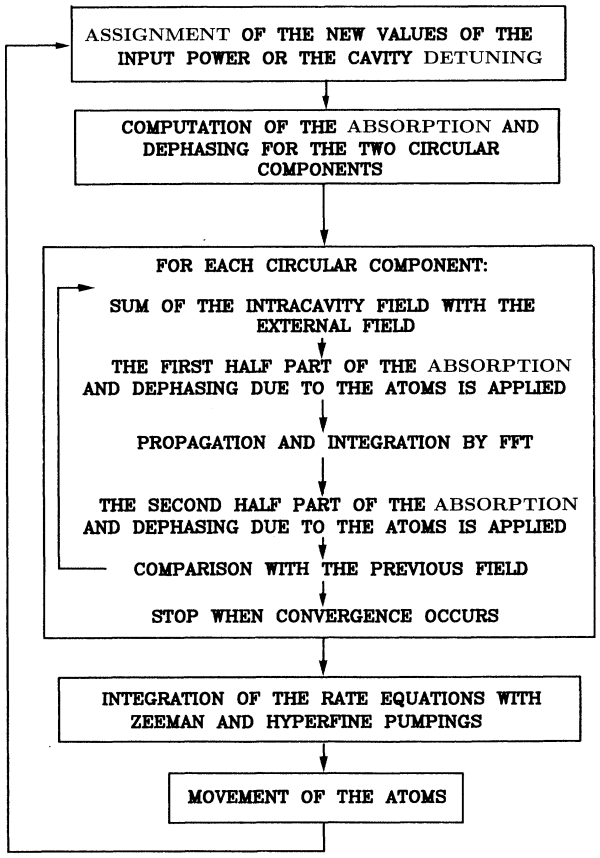


FIG. 15. Scheme of the computation algorithm used by the simulation program.

$m$th iteration, we have

$$U_{m+1}(x)=RF(x)P[F(x)U_m(x)]+\sqrt{T}\,U_{\text{in}}(x)\ , \quad (1)$$

where $R$ is the reflection coefficient at the mirrors, $T$ is the transmission coefficient, $F(x)$ is a complex coefficient encoding transmission and dephasing of the medium for each $x$ coordinate, $P$ is the intracavity propagation operator, and $U_{\text{in}}(x)$ is the input field. In our simulation $U_{\text{in}}(x)$ is Gaussian, with an angle of incidence $\theta$, and a peak amplitude normalized to one, that is,

$$U_{\text{in}}(x)=e^{i(x^2/w^2+x\theta 2\pi/\lambda)}\ . \quad (2)$$

Our attempt to use the methods of Ref. [19] to compute the field inside a planar mirror optical cavity (with a nonzero angle of incidence) was almost without results. In our opinion, that method does not provide the precision required by our problem in computing the focusing effects and it does not produce enough "gain" for the instabilities. The method we have implemented instead uses a more classical computation of the spatial transverse distribution of the field, namely the iteration of the intracavity propagation in the unidimensional Fresnel approximation. The general formula for the propagator operator that gives the field in the same $x$ interval on the input window after a round-trip, in a one-dimensional case, is

$$V_0(\eta\sqrt{\lambda 2L}\,)=e^{i\phi}\frac{(1-i)}{2}e^{i\pi\eta^2}\times\int_{-\infty}^{+\infty}[V(\xi\sqrt{\lambda 2L}\,)e^{i\pi\xi^2}]e^{-2\pi i\eta\xi}d\xi\ , \quad (3)$$

where $\xi=x/\sqrt{\lambda 2L}$, $\eta=x_0/\sqrt{\lambda 2L}$, and $x_0$ is the coordinate where we carry on the computation. The phase $\phi$ is a function of the cavity detuning $\delta_c$ and of a further phase contribution introduced to compensate the effect of a small tilt angle $\theta$

$$\phi=2\pi\left[\frac{\delta_c}{\mathcal{R}_{\text{FSR}}}+\frac{L}{\lambda}\theta^2\right]\ , \quad (4)$$

where $\mathcal{R}_{\text{FSR}}=c/2L$ is the free spectral range of the cavity.

The integration is carried out by means of fast-Fourier-transform computation techniques, and the iteration of Eq. (1) is done independently for the two $\sigma+$ and $\sigma-$ circular components. The input window is taken larger than the beam diameter ($2w$) and is divided for this computation in $n=512$ intervals. The algorithm forces the window to be $\sqrt{\lambda 2Ln}$ wide. Thus, having $2L=26$ cm and $\lambda=589.6$ nm, the sampled window and the intervals are 8.86 mm and 17.3 $\mu$m wide, respectively. The pixels used for the atomic variables are four times larger: $\Delta x=69.2$ $\mu$m. Finally, the atomic velocity to be considered for the comparison with the simulation is the mean velocity of one side of the Maxwellian distribution, $v_m=(2kT/\pi M)^{1/2}$, (where $k$ is the Boltzmann constant, $T$ the temperature, and $M$ the atomic mass). In our case, $v_m=312$ $m$/sec; therefore $\Delta t=0.8\Delta x/v_m=177$ nsec.

On the other hand, to know $F(x)$, we integrate independently the rate equations for the Zeeman and hyperfine pumpings. In both cases, we treat the laser-atom interaction as in a $\Lambda$ system with one excited state and two ground states. For the Zeeman pumping, the well-known rate equation of the normalized orientation $n_Z=(n_+-n_-)/N$ is

$$\dot{n}_Z=P-(Q+\Gamma)n_Z\ , \quad (5)$$

where $P=P_+-P_-$, $Q=P_++P_-$, $P_+$ and $P_-$ are the pumping terms associated with the two circular components, and $\Gamma$ is the relaxation terms for the ground-state polarizations. $n_Z$ runs between $+1$ and $-1$. This equation leads to the general solution

$$n_Z(t)=[n_Z(0)-n_{Zs}]\exp[-(Q+\Gamma)t]+n_{Zs}\ , \quad (6)$$

where $n_{Zs}=P/(Q+\Gamma)$ is the stationary solution. This equation is calculated by finite steps (for each $x_j$ coordinate)

$$n_{Zj}(t_i+\Delta t)=[n_{Zj}(t_i)-n_{Zs}]\exp[-(Q+\Gamma)\Delta t]+n_{Zs}\ , \quad (7)$$

where $t_i=i\Delta t$. A small value is initially given to $n_{Zj}$ to introduce the transient capable of breaking the symmetry and to start the process.

The hyperfine pumping is described separately by analogous rate equations. If $n_h$ is the normalized population difference of the two hyperfine levels of the ground state, we use the integration

$$n_{hj}(t_i+\Delta t)=[n_{hj}(t_i)-n_{hs}]\exp[-(aQ+\Gamma)\Delta t]+n_{hs}\ , \quad (8)$$

with the same meaning of the symbols as before. Here $n_h$ ranges between 0 and 1, and $n_{hs}=aQ/(aQ+\Gamma)$, where $a$ is a small coefficient chosen to make the simulation and the experimental results fit the best. The introduction of $a$ approximates the fact that, in the atomic longitudinal velocity distribution, the atoms that mainly contribute to the hyperfine pumping possess a consistent atomic detuning, so that the effective pumping power "seen" by the atoms themselves is reduced.

The dispersive effect of the polarizations is then approximated by the sum of the hyperfine and the Zeeman contributions, which act differently. The hyperfine polarization produces equal absorption and dephasing on the two circular components of the field, so that ($D$ indicates difference from thermal equilibrium)

$$D\Phi=-\Phi_h n_h,\quad \Phi_h>0\ ,$$

$$DA=-A_h n_h,\quad A_h>0\ ,$$

where $\Phi_h$ and $A_h$ are coefficients for the dephasing and absorption, respectively. Both are proportional to the vapor density and to the cavity length. The Zeeman contribution, instead, is opposite for the two circular components $\sigma+$ and $\sigma-$, so that

$$D\Phi_{Z+}=+\Phi_Z n_Z,\quad DA_{Z+}=-A_Z n_Z \quad \text{for } \sigma+\ ,$$

$$D\Phi_{Z-}=-\Phi_Z n_Z,\quad DA_{Z-}=+A_Z n_Z \quad \text{for } \sigma-\ ,$$

with the absorption and dephasing coefficients $A_Z, \Phi_Z > 0$. Because of the sign of $\Phi_Z$, an intensity unbalance between the circular components of the field gives, together with the spatial dependence, a focusing lens effect for the predominant component and a defocusing effect for the other one.

Finally, the complete expression for the function $F$ of Eq. (1) for the two opposite components $\sigma+$ and $\sigma-$, when the hyperfine ($A_h$) and Zeeman ($A_Z$) absorptions are considered, together with the absorption ($A$) introduced by the vapor at thermal equilibrium, is

$$F_{\pm} = \exp[-A + A_h n_h \pm A_Z n_Z] \exp[i(-\Phi_h n_h \pm \Phi_Z n_Z)] . \tag{9}$$

To facilitate the comparison with the experiment, the parameters $\delta_c$, $\theta$, and $P_{\text{in}}$ are introduced with their real physical dimensions and the pumping coefficients $P$ and $Q$ are calculated as

$$\begin{aligned} Q &= p\frac{2}{\pi w^2} P_{\text{in}}(|U_+|^2 + |U_-|^2) , \\ P &= p\frac{2}{\pi w^2} P_{\text{in}}(|U_+|^2 - |U_-|^2) , \end{aligned} \tag{10}$$

where $p$ is a pumping rate coefficient. Assuming that, in our simplified model, (the mean of) the relative square dipole for the $F=2 \rightarrow F'=2$ transition (that is, $\frac{5}{24}$) is reasonable and taking a detuning of 50 MHz, in units of $\Delta t$, we assumed for $p$ the value 0.091 mm$^2$/mW.

The results of the numerical solution of Eqs. (1), (7), and (8) are given for each instant $t_i$ of time. Triangular scanning of the cavity mistuning $\delta_c$ or of the input power $P_{\text{in}}$ is included. For every scanning, the angle of incidence $\theta$ may be varied. The other parameters, such as absorptions or dephasings, are also entered from the keyboard.

The values of the parameters in the simulations reported here are $\Phi_Z = 1$, $\Phi_h = 1.8$, $A_h = 0.13$, $A_Z = 0.13$, $a = 0.05$, and $\Gamma = 0.03/\Delta t$. They agree with the values we can reasonably expect in the physical situation. Because of the low finesse of our cavity, we assume transmission and absorption coefficients for the mirrors to be both equal to 0.07.

Figure 16 shows examples of curves of one of the two transmitted circular components during a triangular modulation of $P_{\text{in}}$ as a function of $t$ for different values of $\delta_c$. As experimentally observed, polarization switchings, Hopf bifurcations with and without slowing down of oscillations on a stable state are reproduced.

The qualitative agreement between simulated and experimental results is also evident when we compare the simulated bifurcation diagrams shown in Fig. 17 with the experimental ones (Fig. 5). The simulated diagrams are obtained by observing the system, fixing the parameters, and waiting long enough to be able to discriminate the type of behavior so as to avoid dynamical counterfeiting. A small amount of noise (added at each point to $n_z$ with a rms level of $10^{-9}$), simulating experimental noise, has been added to allow the instabilities to start, as the system is in principle mathematically symmetrical. Here the resemblance between the two cases is quite satisfactory, as is also the dependence on the parameters. For $\theta = 0$, the condition of absence of oscillations and the division of the parameter space $P_{\text{in}} - \delta_c$ into two zones, one monostable and the other one bistable, is reproduced. However, at $\theta = 0$, the simulation also presents a situation (which has not been systematically explored) in which the breaking of the polarization symmetry is antisymmetric around $x = 0$ instead of being spatially symmetric. In other words, the field profile may also present a peak at $x > 0$ for the left polarization and one at $x < 0$ for the right polarization or vice versa.

For $\theta$ increasing from zero to about 1 mrad, a region with oscillations arises and, as in the experiment, the oscillation frequency grows with $\theta$ while its amplitude decreases.

The point of intersection of the three bifurcation lines places itself at a $\delta_c$ value near zero and drifts toward larger $P_{\text{in}}$ as the tilt angle is increased, as observed in the experiment. Moreover, the behavior of the simulation is not very sensitive to quite large modifications of all the other parameters involved in the model, so it is robust. In the exploration of the parameter space, the program

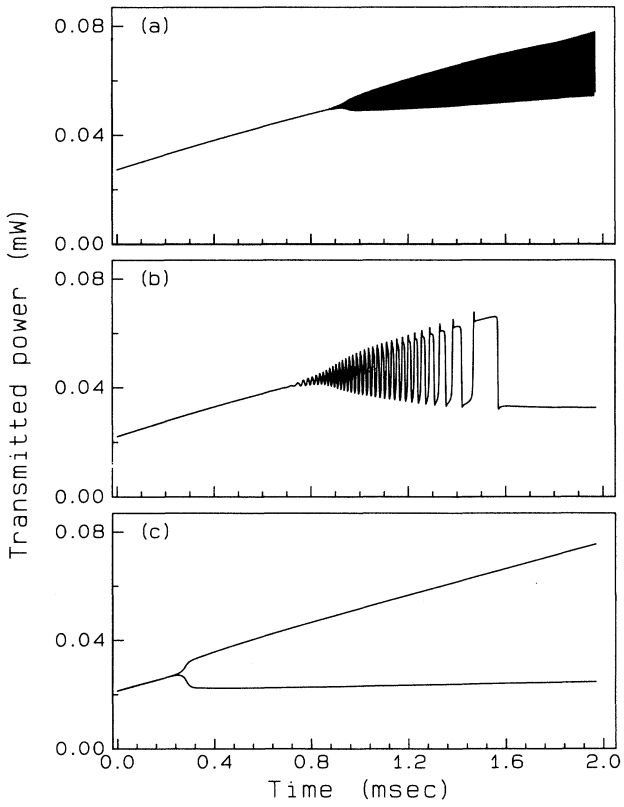


FIG. 16. Simulation of the transmitted power of a circularly polarized component under a linear modulation of $P_{\text{in}}$ from 2.8 to 10 mW (compare with Fig. 2). On the abscissa is the time of the modulation. $\theta = 0.2$ mrad. (a) $\delta_c = -30$ MHz, (b) $\delta_c = -17$ MHz, (c) $\delta_c = -5$ MHz; both components are shown here for a better representation.

runs along the vertical lines alternately in the two directions and, as can be seen, there is a thin hysteresis region on the upper border of the bistable region: this is a sign of a small tristable region that can also be observed in the experiment.

Figure 18 shows a sequence of the simulated spatial distribution of the intracavity field and its evolution in time when oscillations happen: the coincidence between the rising of an orientation and the transmission of a circular component can be easily seen and is due to the focusing effects. It can also be seen that these spatial patterns move like a wave inducing an alternation between peaks and dips, both of orientation and transmitted light.

This succession of pictures shows that the orientation wave of the atoms traveling in the direction of the tilt (toward the right-hand side of every picture) is more pronounced than the other, and we can look at it as the "leading term" of the oscillatory mechanism. In this unbalancing of the contributions from the two directions of motion, the role of the breaking of the spatial symmetry can be visualized. Roughly speaking, for $\theta=0$ a breaking of the polarization symmetry, antisymmetric in space and stationary is allowed, while for $\theta>0$ there is something like the motion of a "barycenter" of the orientation that has a velocity different from zero in the tilt direction: a peak in the orientation wave drags a peak in the field profile in the same direction, followed by another one with an opposite polarization. This last, in turn, grows another peak with opposite orientation, and so on. The asymmetry in the orientation waves originated by the tilt is amplified because the atomic wave traveling in the direction of the tilt remain in phase with the field and is therefore enhanced with respect to the other wave.

As can be seen, the simulation is able to reproduce satisfactorily all the principal features of the experiment, and all the parameters are in good agreement with the experimental ones. If we consider the high degree of simplification adopted in this simulation and nevertheless its capacity to perform the essential behavior of the system, it is legitimate to maintain that the mechanism based on the atomic motion must be the predominant one in the observed phenomenology.

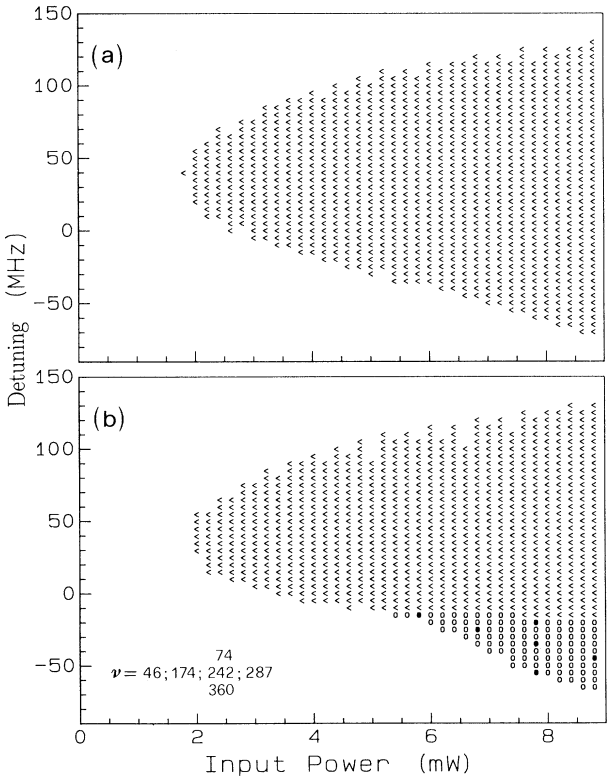


FIG. 17. Simulated bifurcation diagrams. < symbols are for bistability, ○ for oscillations, no symbol for monostability. (a) $\theta=0$, (b) $\theta=0.2$ mrad. The frequency values (in kHz) shown in (b) refer to the ●, in the same order from left to right and from top to bottom.

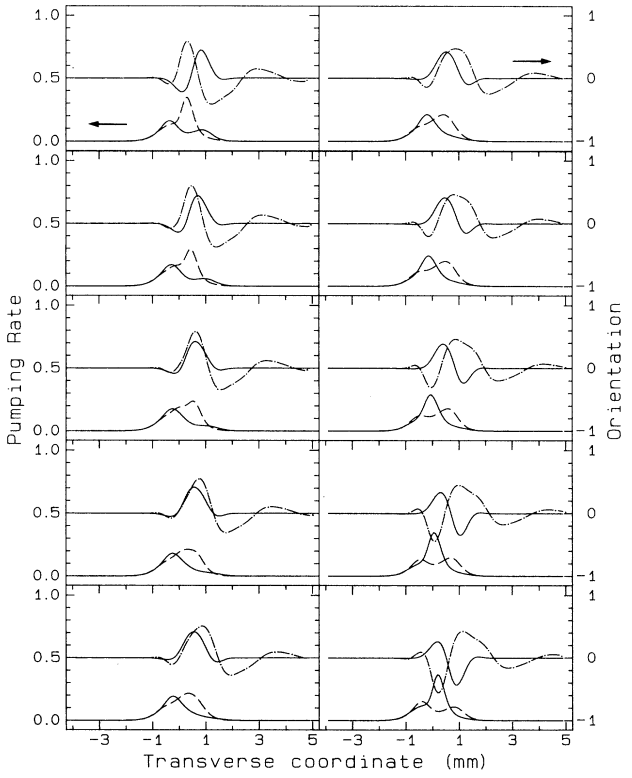


FIG. 18. Simulation of the spatial transverse distribution and time evolution of orientation and field inside the FP during half a period of oscillation. In each plot the two lower curves are the intracavity pumping rates ($P_+$,$P_-$) for the two opposite circular polarizations (to be read on the left scale); they are normalized to the time step $\Delta t$ of computation. The two upper curves are the orientations for the atoms traveling in the two opposite directions (right scale). $P_{in}=8.7$ mW, $\delta_c=-24$ MHz, $\theta=0.2$ mrad. Every picture is taken three time steps after the former; the temporal succession is from top to bottom and from left to right.

## VI. CODIMENSIONALITY

It is well known that, apart from more complex mathematical implications, the word "codimension" (of a bifurcation) denotes the minimum number $k$ of parameters for which a given bifurcation stably occurs. Examples of bifurcations of codimension one are the symmetrical pitchfork and Hopf bifurcations, which depend on just one parameter. When $k>1$, a bifurcation point is called a multiple bifurcation point of codimension-$k$. In practice, let us suppose we are dealing with a physical system depending on a certain number of independent parameters that exhibits a bifurcation when just a minimum subset of the parameters involved are varied. This bifurcation is "robust" or "persistent" if it still occurs when the other parameters are perturbed. The codimension of this bifurcation is given by the number or parameters composing the given subset, so that it is also the smallest dimension of the parameter space which contains the bifurcation in a persistent way.

As shown in Fig. 5 for our experimental system, if $\theta$ is different from 0, the plane of the parameters $P_{\text{in}}$ and $\delta_c$ is divided into different regions by lines of bifurcations. These are a line of PB or PS (in this second case there would be two lines), a line of HB, together with a line crossing where the system apparently passes from an oscillatory state (limit cycles) to a bistable state, or vice versa. These lines are of codimension-one and seem to converge in a very restricted region toward a point. $P_{\text{in}}$ and $\delta_c$ are to be simultaneously adjusted to reach this point. This bifurcation diagram is very reproducible and is not sensitive to perturbation of other parameters such as sodium temperature or density, laser frequency, laser beam diameter, and wave-front radius. Moreover, if $\theta$ is not 0, there is no sensitivity to perturbations of the incidence angle or to external spatial breaking of the symmetry. Some attention must be devoted to the external magnetic field and to the polarization of the incident beam. The whole phenomenology is strongly affected by even small perturbations of the situation with exact zero magnetic field and perfect linear polarization of the incident laser light. However, we can consider these particular conditions of equilibrium as "boundary conditions" to impose a "symmetry" between the pumping power of the two circular components of the incident light, and therefore we have a balanced competitive phenomenon inside the cavity. Within this framework we can say that with just the two parameters $P_{\text{in}}$ and $\delta_c$ we are able to characterize and determine the whole phenomenology of bifurcations, which can thus be described in a plane of these two parameters. In particular, the presence of the intersection of the different bifurcation lines persists. This means that there must exist a multiple bifurcation point of codimension-two. Theory [26] tells us that similar points, though theoretically expected, are in fact very difficult to observe because of the noise in every physical system: they can only be "approached."

The same theory [26] provides a classification of the expected behaviors around points of multiple bifurcations of codimension-two. Our case is very similar to the one in which the Jacobian matrix of two differential equations possesses a double 0 eigenvalue, together with a superimposed $\pi$ symmetry. It can be shown that this case can be modeled as

$$\dot{x}=y, \quad \dot{y}=ax+by\pm x^3+x^2y \ , \tag{11}$$

corresponding to the second-order equation

$$\ddot{x}=(b+x^2)\dot{x}+(\pm x^2+a)x \ , \tag{12}$$

where we have both a Van der Pol and a Duffing term. Its linearization around $(x,y)=(0,0)$ yields a Jacobian with a double 0 eigenvalue.

Stability analysis near $(x,y)=(0,0)$ gives the two bifurcation diagrams of Fig. 19 (see again [26]). The two signs of the cubic term both hint at the occurrence of a stable state (monostability), which can become a saddle point or a limit cycle. Such behaviors are very similar to our experiment. In particular, case (b) would require a collapsing of the limit cycle on a stable state inside the amplitude of the orbit (in the phase space), at least in the proximity of the origin. Instead, we clearly experimentally observe a stable state outside the oscillation amplitude when they abruptly cease.

The case with a positive cubic term [Fig. 19(a)] can fit better if a tristable region near the origin is present (Fig. 20). We have experimental indications of this zone, but it is too small to be easily checked. In particular, OT seems more evident if $\theta$ if very close to zero. So we could have, near the aforementioned codimension-two bifurcation point, another point of convergence of three lines which separate a zone of monostability, one of bistability and one of tristability. Otherwise, this tristable zone may extend as a thin border between the monostable and the bistable region. The behavior of the system in the neighborhood of the codimension-two point could be described by a static potential of sixth degree (see [27]).

We have managed to reconstruct this behavior with the aid of the simulation program. An enlargement of the simulated bifurcation diagram in the region near the origin reproduces a very small tristable zone, as expected (Fig. 21). Every point has been characterized by waiting for a time much longer than in the case of Fig. 17. The noise level had been progressively lowered to reduce its effect on the bifurcation lines. We believe that the bifur-

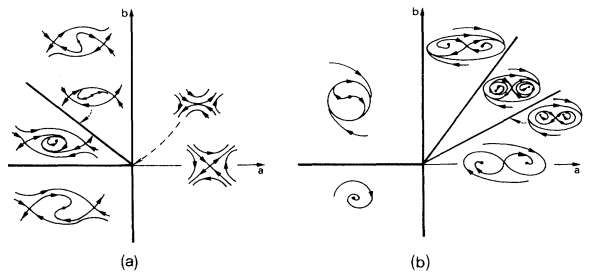


FIG. 19. Theoretical bifurcation diagrams for a double zero eigenvalue (of the linear associated part of a flow). (a) The case with the positive $x^3$ term. (b) The case with the negative $x^3$ term. The arrows indicates the direction of motion in the phase space.

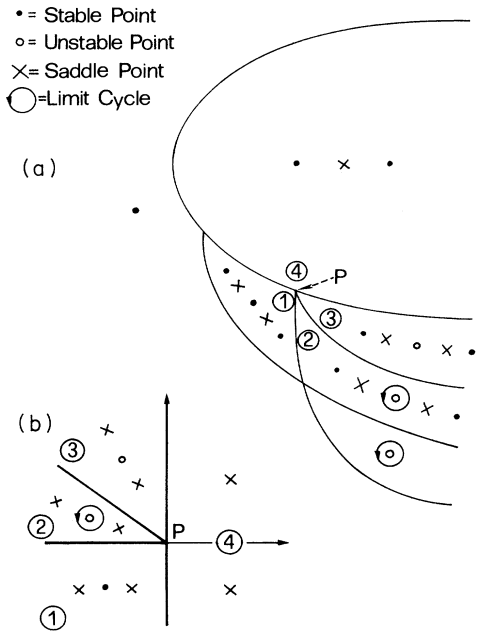


FIG. 20. (a) Reconstruction of the experimental bifurcation diagram with the addition of a tristable region (1). (2) is the coexistence of a limit cycle and two stable state. (3) is the breaking of the limit cycle on the saddle point. (4) is the bistable state. $P$ is the point of multiple bifurcation of codimension 2. (b) Scheme of behavior around $P$ [to be compared with Fig. 14(a)].

cation lines in the figure would not change any more by a further lowering of the noise, with the possible exception of the thin tristable region on the extreme left of the figure: a further investigation would require very long computing times.

Moreover, it is possible to plot suitable variables to

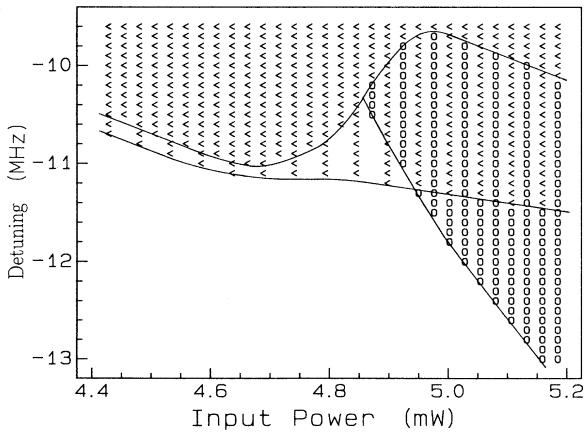


FIG. 21. Enlargement of a simulated bifurcation diagram in the neighborhood of the intersection of the different bifurcation lines: symbols are the same as in Fig. 17. The program runs along the vertical lines alternately in the two directions. In the triangular central region, where it exhibits hysteresis between bistable and monostable state, there is tristability.

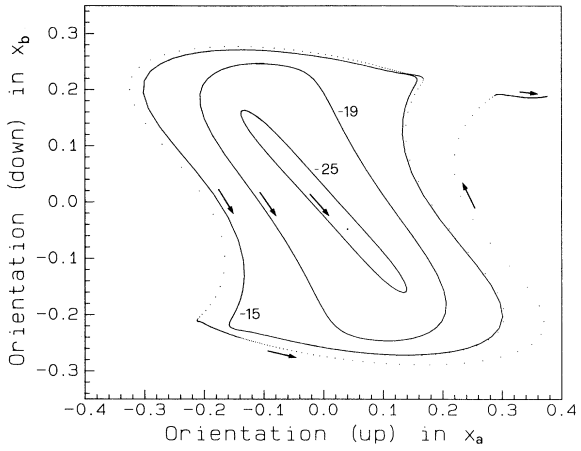


FIG. 22. Limit cycles in the phase space for three detuning values (aside each curve in MHz). The variables $x$ and $y$ are the spin orientations, in two different spatial pixels $x_a=0.15$ mm, $x_b=0.84$ mm, of the atoms moving in the two opposite directions ("up" and "down"). The dotted curve shows the modification of a stable limit cycle when the detuning is linearly varied from $-15$ to $-9$ MHz during an interval of $\approx 0.1$ msec: the limit cycles become unstable and then break down on a fixed point. The arrows show the direction of motion along the curve. $P_{in}=7$ mW; $\theta=0.2$ mrad.

reconstruct trajectories in the phase space; as is shown in Fig. 22, the limit cycle breaks down on a stable state which is situated outside the amplitude of the orbit, as experimentally observed. The same orbit is very similar to a heteroclinic one, that is, a closed trajectory connecting (two) different fixed points. This means that the model simulates the passage from the limit cycle to the stable state through a heteroclinic orbit. The same behavior is required in the cubic positive term case, which has in this way a further confirmation. It must be pointed out that this result provides the same behavior for the local spatial variables, e.g., the transmitted intensities, as for the global ones, such as the total transmitted power.

Summarizing, we have found consistency between the experimental results and a numerical simulation together with a theoretical dynamical scheme of behavior.

## VII. CONCLUSION

In this work, we have shown that a linearly polarized laser beam, tuned to the center of the sodium $D1$ line, can exhibit, by crossing a Fabry-Pérot cavity filled with free sodium atoms, a variety of bifurcations: toward $\sigma+$ ($\sigma-$) polarization or toward an oscillatory behavior between the same two circular polarizations, depending on the input power, the cavity detuning, and the angle of incidence of the beam on the mirrors. Moreover, spatial transverse effects have been observed in the transmitted profile of the beam. The main intracavity processes are Zeeman and hyperfine pumpings, which account for polarization-dependent self-focusing and self-defocusing. This modifies the cavity stability behavior because of the delay effect provided by the atomic motion. A simplified

model, based on these mechanisms, reproduces satisfactorily the main observed features. On the other hand, the instabilities could be thought of in terms of a gain-feedback mechanism, where gain is provided by opposite effects (enhanced by the cavity) on the $\sigma+$ and $\sigma-$ polarizations, namely the focusing of one component and the defocusing of the other one, and delayed feedback is provided by the atomic motion. It is an open question if the observed oscillations could be conveniently treated in terms of wave mixing, as described in [28], where the competition between two orthogonal polarizations is considered, but not the atomic motion, which instead we believe to be a crucial element.

A very important result is that both the experimental bifurcation diagrams and the simulated ones show that oscillations occur only when the angle of incidence of the beam on the mirrors is different from zero. In fact, with normal incidence, we have only PB or PS. Furthermore, the phase analysis of the transverse profiles of the transmitted beams shows, in connection with the oscillatory behavior, a periodic stripe pattern in the spatial distribution of the atomic orientation. An intrinsic breaking of the O(2) symmetry of the cavity, due to the cavity itself, defines a preferential transverse direction. So it is the external breaking of the residual symmetry $Z_2$ that may give rise to the oscillatory behavior and to pattern formation.

Both the experimental and the simulated bifurcation diagrams show different bifurcation lines converging toward a codimension-two bifurcation point. In the neighborhood of this point, the behavior is described by a second-order differential equation, which lead to heteroclinic orbits in particular conditions. This behavior is evident both in the experiment and in the numerical simulation. It suggests that the phenomenology, whose physical mechanisms have been verified in our numerical simulation, could also have an analytical or semianalytical description. In particular, it can be thought that a differential equation of the second order, perhaps with potential terms of order greater than three, might give a global description of the bifurcation diagram, including a small tristable region. This could be very important in order to clarify the role of the spatial symmetry breaking in this problem. Similarity with other experimental results [29], together with theoretical investigations [1,19,30] which hold for different physical mechanisms, suggest the possibility of a more general description, independent of the specific physical system we are dealing with.

## ACKNOWLEDGMENTS

This work is partially supported by the contract ESPRIT-7118TONICS of the European Economic Community. We are affectionately grateful to P. Salieri, who stimulated this work. We also thank F. T. Arecchi, A. Politi, J. Tredicce, and P. Chossat for fruitful discussion, D. Iorio for his contribution in the computation of the intracavity field, G. Giacomelli and G. P. Puccioni for their help with the computers, S. Mascalchi for the electronics of the Nipkow disk, and S. Acciai, M. D'Uva, A. Tenani, and P. Bianchi for their technical assistance.

[1] N. B. Abraham and W. J. Firth, J. Opt. Soc. Am. B **7**, 951 (1990).
[2] L. A. Lugiato, Phys. Rep. **219**, 293 (1992).
[3] W. J. Sandle and A. Gallagher, Phys. Rev. A **24**, 2017 (1981).
[4] F. T. Arecchi, G. Giusfredi, E. Petriella, and P. Salieri, Appl. Phys. B **29**, 79 (1982).
[5] S. Cecchi, G. Giusfredi, E. Petriella, and P. Salieri, Phys. Rev. Lett. **49**, 1928 (1982).
[6] M. W. Hamilton, W. J. Sandle, J. T. Chilwell, J. S. Satchell, and D. M. Warrington, Opt. Commun. **48**, 190 (1983).
[7] W. E. Schultz, W. R. MacGillivray, and M. C. Standage, Opt. Commun. **45**, 67 (1983).
[8] J. Mlynek, F. Mitschke, R. Deserno, and W. Lange, Phys. Rev. A **29**, 1297 (1984).
[9] E. Giacobino, Opt. Commun. **56**, 249 (1985).
[10] M. Kitano, T. Yabuzaki, and T. Ogawa, Phys. Rev. A **24**, 3156 (1981).
[11] F. Mitschke, J. Mlynek, and W. Lange, Phys. Rev. Lett. **50**, 1660 (1983).
[12] M. Kitano, T. Yabuzaki, and T. Ogawa, Phys. Rev. A **29**, 1288 (1984).
[13] T. Yabuzaki, T. Okamoto, M. Kitano, and T. Ogawa, Phys. Rev. A **29**, 1964 (1984).
[14] F. Mitschke, R. Deserno, W. Lange, and J. Mlynek, Phys. Rev. A **33**, 3219 (1986).
[15] I. Bar Joseph and Y. Silverberg, Phys. Rev. A **36**, 1731 (1987).
[16] J. Nalik, W. Lange, and F. Mitschke, Appl. Phys. B **49**, 191 (1989).
[17] J. Nalik, L. M. Hoffer, G. M. Lippi, Ch. Vorgerd, and W. Lange, Phys. Rev. A **45**, R4237 (1992).
[18] C. M. Savage, H. J. Carmichael, and D. F. Walls, Opt. Commun. **42**, 211 (1982).
[19] M. Haelterman and G. Vitrant, J. Opt. Soc. Am. B **9**, 1563 (1992); see also M. Haelterman, G. Vitrant, and R. Reinisch, *ibid.* **7**, 1309 (1990).
[20] G. Giusfredi, P. Salieri, S. Cecchi, and F. T. Arecchi, Opt. Commun. **54**, 39 (1985).
[21] P. Salieri, G. Giusfredi, S. Cecchi, and F. T. Arecchi, J. Opt. Soc. Am. B **5**, 1166 (1988).
[22] G. Giusfredi and R. Hostetler, Rev. Sci. Instrum. **60**, 598 (1989).
[23] A. Moretti and F. Strumia, Phys. Rev. A **3**, 349 (1971).
[24] A. Omont, Prog. Quantum Electron. **5**, 69 (1977).
[25] M. Ducloy, Phys. Rev. A **8**, 1844 (1973).
[26] J. Guckenheimer and S. P. J. Holmes, *Nonlinear Oscillations, Dynamical Systems and Bifurcations of Vector Fields,* Applied Mathematical Science Vol. 42 (Springer-Verlag, New York, 1983).
[27] M. Kitano, T. Yabuzaki, and T. Ogawa, Phys. Rev. Lett. **46**, 926 (1981).
[28] G. Grynberg, M. Vallet, and M. Pinard, Phys. Rev. Lett.

**65**, 701 (1990).
[29] G. Grynberg, Opt. Commun. **66**, 321 (1988); see also G. Grynberg, E. Le Bihan, P. Verkerk, P. Simoneau, J. R. R. Leite, D. Bloch, S. Le Boiteaux, and M. Ducloy, *ibid.* **67**, 363 (1988); A. Petrossian, M. Pinard, J. Y. Courtois, and G. Grynberg, Europhys. Lett. **18**, 689 (1992).
[30] W. J. Firth, A. Fitzgerald, and C. Paré, J. Opt. Soc. Am. B **7**, 1087 (1990).